

6B.6 ATTEMPTS TO OBSERVE POLARIMETRIC SIGNATURES OF RIMING IN STRATIFORM PRECIPITATION

Jonathan M. Vogel*, Frédéric Fabry, and Isztar Zawadzki

Department of Atmospheric and Oceanic Sciences, McGill University, Montreal, QC, Canada

1 INTRODUCTION AND BACKGROUND

Now that the upgrade of all National Weather Service WSR-88D radars to dual-polarization is complete, a larger variety of weather systems are observed on a daily basis. Some recent studies have focused on polarimetric signatures of microphysical growth processes above the bright band in stratiform precipitation (e.g., Kennedy and Rutledge, 2011; Andrić et al., 2013), Z_{DR} columns in convective storms (e.g., Illingworth et al., 1987; Kumjian et al., 2014), and hydrometeor refreezing (Kumjian et al., 2013).

Stratiform precipitation is generally more widespread and spatially uniform than convective precipitation. The most identifiable feature of stratiform precipitation is the distinct presence of a reflectivity bright band as ice crystals melt at the 0°C level (Fabry and Zawadzki, 1995, 2000; Zawadzki, 2013). Above the melting layer, ice crystals grow by complex processes that depend on temperature, moisture content, updraft, and fall speeds. The main growth processes are vapor deposition, aggregation, and riming. Bailey and Hallett (2009) have shown that, depending on temperature and supersaturation with respect to ice, depositional growth of crystals may form shapes varying from dendritic and plate-like to columnar to bullets and rosettes.

Previous studies have routinely observed the presence of a local maxima in Z_{DR} around the -15°C region often concurrent with a local minima in ρ_{HV} (Kennedy and Rutledge, 2011; Andrić et al., 2013; Bechini et al., 2013; Schneebeli et al., 2013). This region corresponds with a maxima in depositional growth rates shown in Figure 5.6 of Byers (1965) and Figure 9.4 of Rogers and Yau (1989), so it has been suggested that these signatures are due to the production and growth of dendritic crys-

tals since this is a favored crystal shape at this temperature. As crystals fall and grow larger, the dominant growth mechanism transitions to aggregational growth. With aggregational growth, crystals grow in size, producing an increase in reflectivity, while becoming more sphere-like and less dense, decreasing Z_{DR} , and decreasing the variety of shapes perceived by the radar, increasing ρ_{HV} .

While depositional and aggregational growth mechanisms have been inferred from polarimetric signatures, observation and detection of riming on a large scale continues to be a challenge. Riming implies the presence of supercooled liquid water (SCLW), which can be dangerous for aviation. To achieve riming, local changes to thermodynamics and microphysics must be present; particularly, local updrafts can produce an excess in available moisture beyond what existing snow can use by deposition leading to the formation of SCLW (Zawadzki et al., 2000). Identification of these regions could also have implications for data assimilation or model microphysics above the melting layer.

A common remote sensing method to infer the presence of riming is by observing changes in fall speed. Unrimed individual crystals rarely fall faster than 1.5 m s⁻¹ while unrimed aggregates will not fall faster than 2.0 m s⁻¹ (Barthazy and Schefold, 2006; Brandes et al., 2008). Several studies have shown that rimed particles will fall at speeds from 1.5 to 2.5 m s⁻¹ or faster (e.g., Mosimann et al., 1993; Mosimann, 1995; Barthazy and Schefold, 2006). Additionally, a riming environment may lead to the formation of secondary ice by rime splintering and/or supercooled drizzle, both of which may produce a bimodal velocity spectra (Hallett and Mossop, 1974; Zawadzki et al., 2001). In this study, we attempted to link regions of riming identified by vertically pointing radar to the corresponding polarimetric signatures from scanning radar.

*Corresponding author address: Jonathan M. Vogel, Atmospheric and Oceanic Sciences, Burnside Hall 805 Sherbrooke Street West, Montreal, QC, Canada, H3A 0B9, e-mail: jonathan.vogel@mail.mcgill.ca

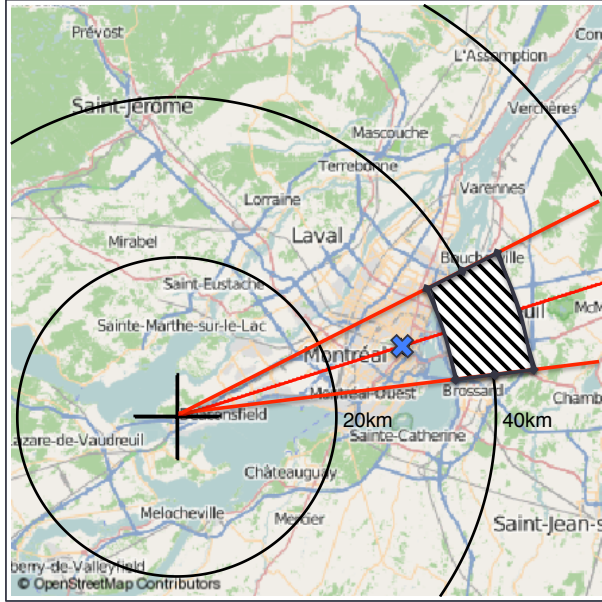


Figure 1: Region of observation east of the McGill S-band radar. The blue X designates the location of the VertiX radar. The red lines mark the 62, 72, and 82° azimuths. The hatched area shows the region in which the polarimetric variables are averaged. The map is used under the Open Database License from www.openstreetmap.org.

2 RADAR DESCRIPTIONS

At the J.S. Marshall Radar Observatory in Ste-Anne de Bellevue, Quebec we have an array of radars at our disposal. Located at the observatory, the McGill S-band radar is a scanning dual-polarization radar which completes a full scan of 24 elevations from 0.5° to 34.4° every 5 minutes. There are also two vertically pointing X-band radars (VertiX), one located at the observatory and another located at the McGill University campus in downtown Montreal, Quebec. Technical details of the VertiX radars can be found in Zawadzki et al. (2001). For this study, we utilized the McGill S-band and the downtown VertiX radars.

2.1 VertiX

Potential riming cases are first identified by using the VertiX radar products, including: reflectivity, Doppler velocity, and 2-minute velocity spectra. Because air density decreases with height, air resistance against a falling particle will be smaller at higher altitudes than at lower altitudes. To correct for this, fall speeds are adjusted to their expected value at 1000 mb using the RUC sounding adapted from eq. (2) in Zawadzki et al. (2005). All further ref-

erences to VertiX Doppler velocity or fall speed assume this adjusted value unless stated otherwise.

As previously mentioned, the two most common signatures of riming are high fall speeds (we assume those with $V_f \geq 2.0 \text{ m s}^{-1}$) and bimodal velocity spectra. Cases with fall speeds slower than 2.0 m s^{-1} and no bimodal spectra are assumed to have insignificant riming, classified as Group 0. Cases with expected riming are separated into two groups: (1) those with $V_f \geq 2.0 \text{ m s}^{-1}$ and no bimodal spectra and (2) those with observed bimodal spectra. It should be noted that cases that fall into Group 2 may have fall speeds slower than 2.0 m s^{-1} , but the rate of velocity increase associated with the primary spectra mode is indicative of riming.

2.2 McGill S-band

After cases are selected using the VertiX radar, the S-band polarimetric data for a given time is averaged over the region shown in Figure 1. The location of VertiX is at about 72° in azimuth and 29 km in range (marked with an X in Figure 1); however, due to its proximity to Mount Royal we looked slightly further down radial to decrease the ground clutter contamination. The region used is between azimuths 62 and 82°, for a near width of about 12 km and a far width of about 15 km, and 35 and 45 km in range. Because polarimetric observations can be noisy, averaging over a region of this size should help to reduce the noise and measurement errors. Additionally, since the cases chosen are generally wide spread stratiform, the microphysical processes should be long lived and spatially homogenous, the shortest period of riming included in this study lasting 45 minutes.

To remove ground clutter and noise contamination, any pixels with $Z < 0 \text{ dBZ}$, $\rho_{HV} < 0.90$, or a target ID of “ground echo” or “biological” are removed. For averaging, the height above ground level is calculated for each pixel and then the data are averaged by height in 200 m increments. So, for example, any pixel within the region between 1.0 and 1.2 km height would be included in the same averaged data point. These averages are calculated for each volume scan, i.e., every 5 minutes.

Because the region in Figure 1 is not collocated with VertiX, the timing of the events may not directly match. To remedy this, the VertiX data is given a time shift to match the S-band data by visually coordinating the reflectivity product of both radars, such as by matching the beginning or ending of high Z periods, columns of Z above the bright band, etc. This allows for direct comparison of riming onset

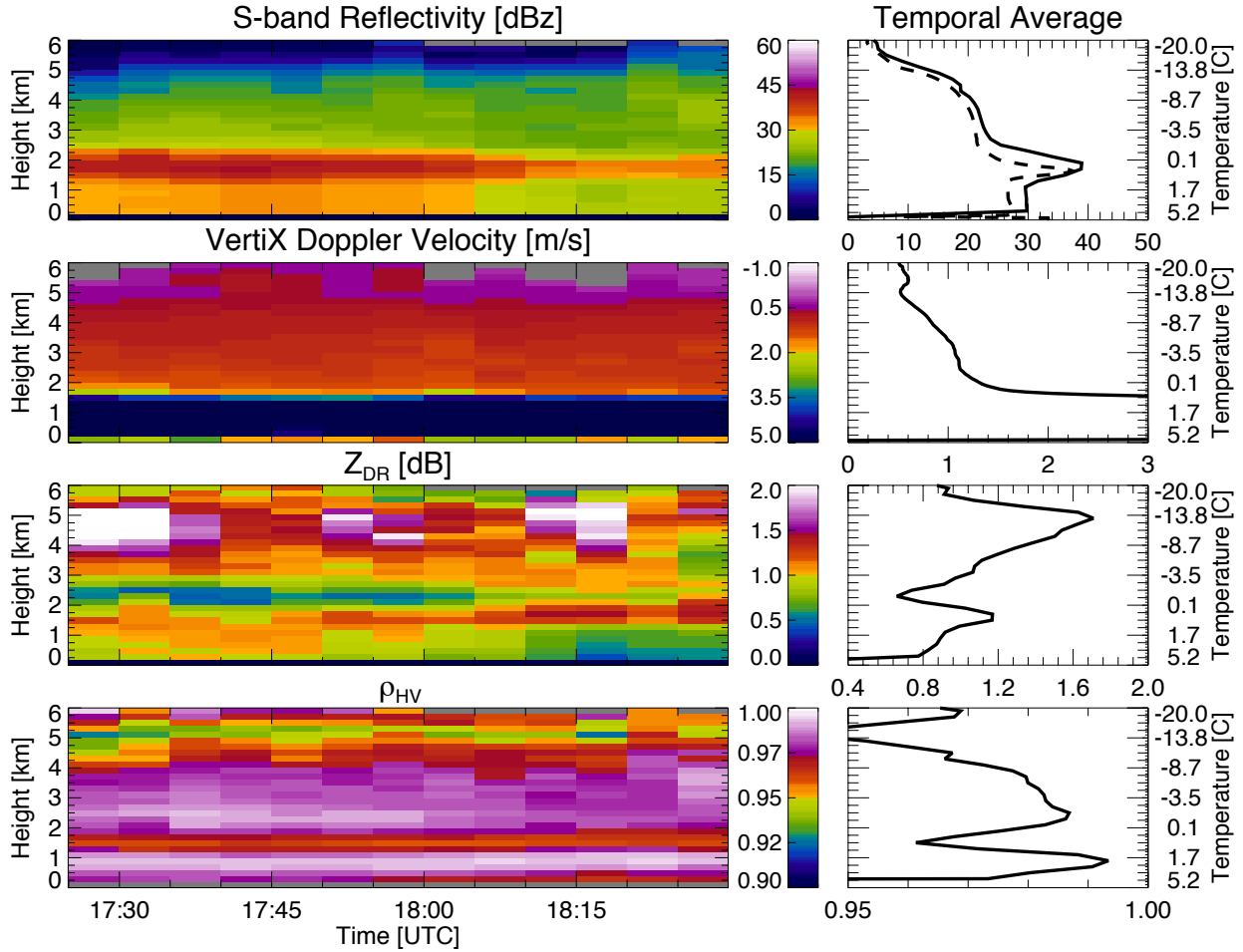


Figure 2: Radar observations for an example of a Group 0 case from 1724-1829 UTC April 21, 2012. The times given are the observation time of the S-band; the VertiX data has been shifted by 10 minutes to match precipitation timing between the two locations. The S-band values plotted have been averaged over the region shown in Figure 1 for each volume scan. The VertiX values plotted have been averaged over a 5 minute interval to match the temporal resolution of the S-band data. The left column shows the data for each volume scan while the right column is the data averaged over the entire period. Temperatures shown are from the RUC sounding for Montreal. The averaged reflectivity profile in the right column shows both observations from S-band (solid line) and VertiX (dashed line).

observed on VertiX with any polarimetric signatures seen on the S-band. Also, this allows for flexibility in time matching as each event is unique and may have different ground speeds.

Since Z_{DR} may drift with time due to both environmental and hardware factors, it must be checked regularly for consistency. Because our S-band radar cannot point vertically, another method must be used. As suggested by Holleman et al. (2010), using the sun is an ideal method for this. By observing the Z_{DR} of the sun we can correct for fluctuations of Z_{DR} on a given day.

3 RADAR OBSERVATIONS

Using the VertiX radar, stratiform weather events were identified as surface rain with an observable bright band or surface snow with little to no upward vertical motion. Cases were then divided into one of the three groups presented above based on the presence of riming or lack thereof. A total of 63 hours of precipitation were used with 31 hours comprising Group 0, 12 hours in Group 1, and 20 hours in Group 2.

3.1 Group 0: non-riming cases

Non-riming cases comprise events where snow fall speeds do not reach 2.0 m s^{-1} and a bi-

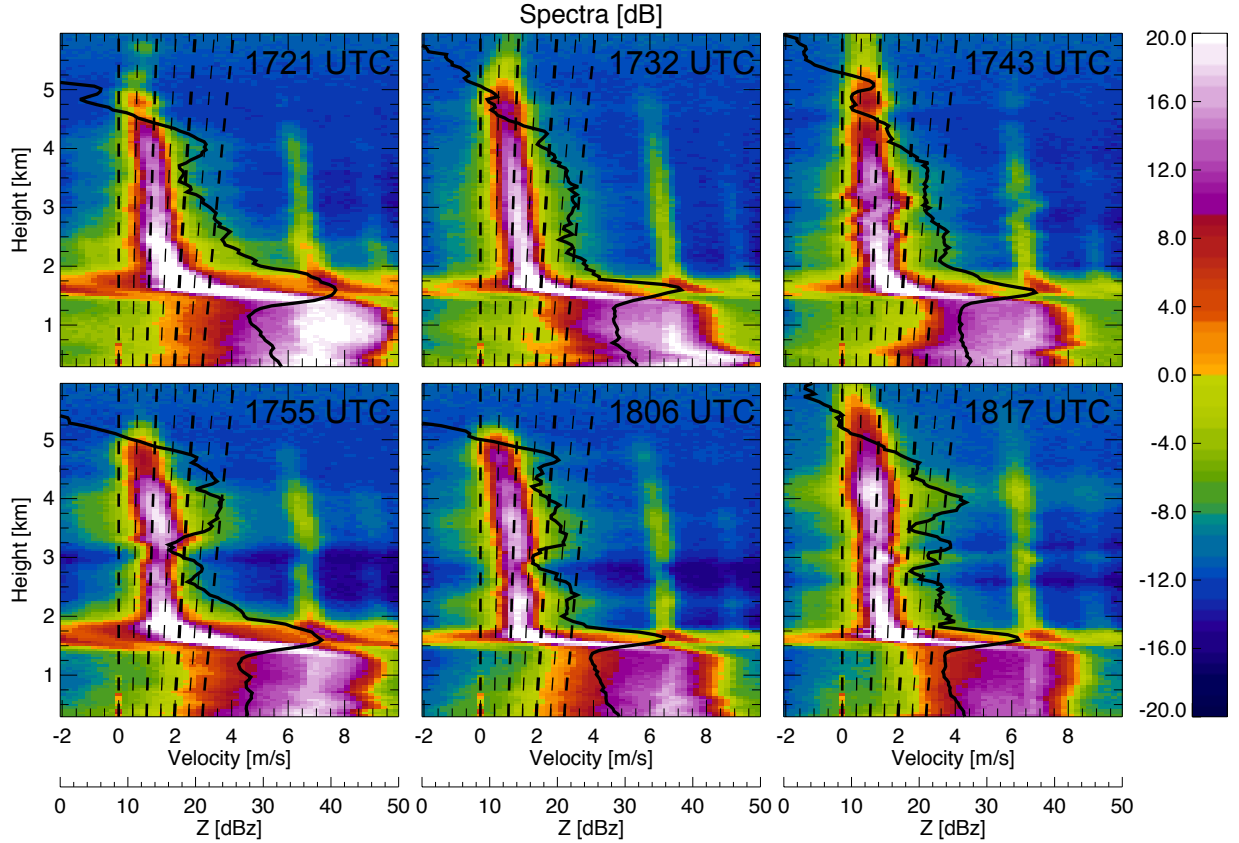


Figure 3: Selected two minute velocity spectra from VertiX for the Group 0 example presented in Figure 2. The times given are the observation time at the VertiX. The velocity spectra displayed is the uncorrected values observed by the VertiX; density corrected fall speeds are shown by the black dashed lines between 0.0 and 3.0 m s⁻¹ in 0.5 m s⁻¹ intervals. The solid black lines are the VertiX observed reflectivity for the same period. Please note the signature around 6.0 m s⁻¹ in snow (and higher values in rain) is due to sidelobes.

modal velocity spectra is not observed. While small amounts of riming could be present, it is too little to be detected without in situ observations. Figure 2 shows an example of the observations of S-band Z , Z_{DR} , and ρ_{HV} , and VertiX Doppler velocity for a typical non-riming event from 1724-1829 UTC on April 21, 2012. The corresponding VertiX velocity spectra are presented in Figure 3. The profiles for Group 0 events follow the observations presented in numerous previous studies (e.g., Kennedy and Rutledge, 2011; Andrić et al., 2013; Bechini et al., 2013; Schneebeli et al., 2013).

At cloud top, ice nuclei are activated at some altitude forming small, quasi-spherical crystals where reflectivity initially increases. In this case, it occurs at temperatures at or below -20°C . Around the -15°C region, the vertical gradient of Z increases, Z_{DR} reaches a local maxima, and ρ_{HV} reaches a local minima. The enhanced depositional growth

rates lead to increased single crystal growth in this region. Individual crystals will fall with their largest axis generally parallel to the ground, so depositional growth would increase Z due to the increase in size while enhancing Z_{DR} due to their shape. A variety of existing and new particles along with their differing growth rates would lead to a reduction in ρ_{HV} . Below this region, Z_{DR} decreases while ρ_{HV} , Z , and fall speed all increase; this coincides with the transition of the dominant growth mechanism from deposition to aggregation as crystals become large enough. Aggregation will increase the size of snowflakes, thereby increasing Z , while trending the shape to be less anisotropic and reducing density, which would decrease Z_{DR} . By collecting ice crystals, aggregation will reduce the variety of particle shapes which will increase ρ_{HV} . Finally, around 0°C , expected signatures of the bright band are observed as the crystals begin to melt (Ryzhkov and

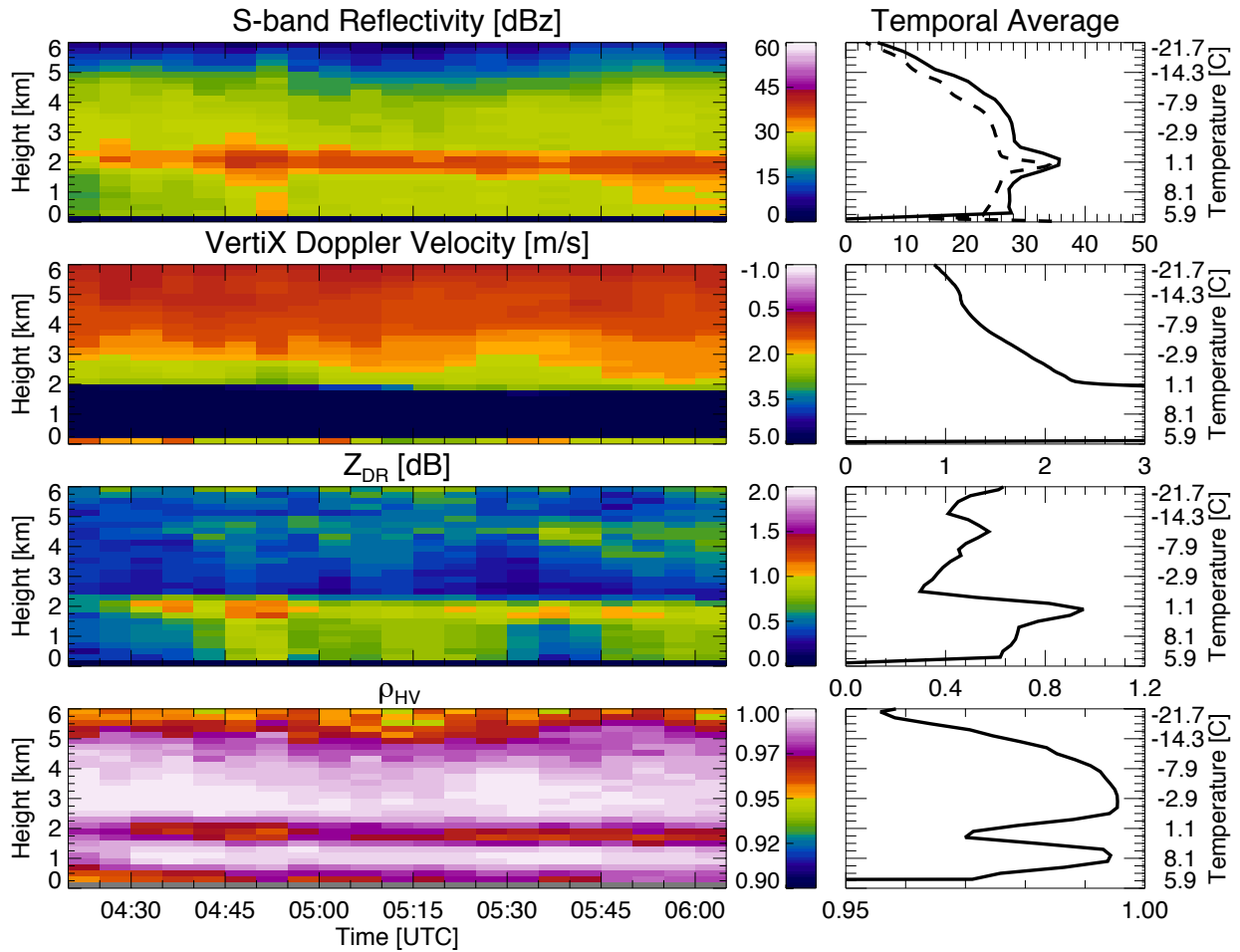


Figure 4: Similar to Figure 2 but for an example of a Group 1 case from 0419-0604 UTC March 12, 2013. The VertiX data has been shifted by 15 minutes to match precipitation timing between the two locations.

Zrnica, 1998).

3.2 Group 1: riming without bimodal spectra

Riming cases in this group are those where no bimodal spectra is observed on VertiX but the fall speed reaches or exceeds 2.0 m s^{-1} . These cases assume riming is taking place without production of any new ice crystals. Figure 4 shows an example of a typical riming event without bimodal spectra from 0419-0604 UTC on March 12, 2013. The corresponding VertiX velocity spectra is presented in Figure 5.

For a riming event without the presence of bimodal spectra, the vertical profiles of radar observations are generally similar to a Group 0 event as presented above. Around the -15°C region, the vertical gradient of Z increases while the signatures of Z_{DR} and ρ_{HV} are present, but less pro-

nounced than in the non-riming case. Below, Z and ρ_{HV} increase while Z_{DR} decreases as growth transitions to aggregation. Below the -5°C altitude, fall speeds increase above 2.0 m s^{-1} while Z_{DR} continues to decrease to values lower than those observed in Group 0 cases. Finally, as the crystals melt near 0°C , bright band polarimetric signatures similar to Group 0 are observed; however, the reflectivity peak is weaker for this case, which has been previously documented for riming events (Fabry and Zawadzki, 1995, 2000).

While Z_{DR} signatures are observed at altitudes where fall speeds indicate riming, it should also be noted that throughout the profile Z_{DR} values are generally lower than during Group 0 events during which fall speeds are also higher. For example, for the Group 0 case, Figure 2 shows at 5 km a Z_{DR} peak greater than 1.6 dB corresponding with a fall speed of about 0.5 m s^{-1} . For this case, at a simi-

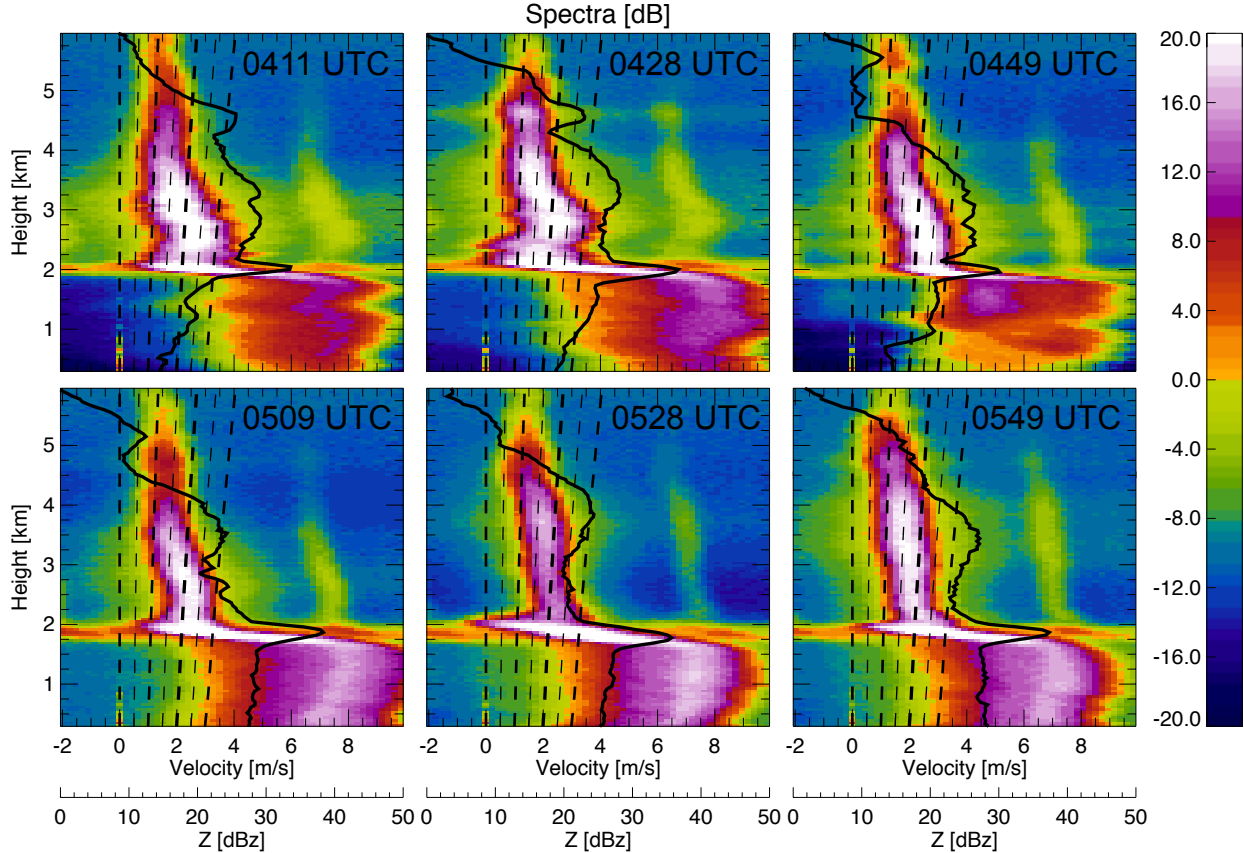


Figure 5: Similar to Figure 3 but for the Group 1 example presented in Figure 4.

lar temperature, Figure 4 shows at 4.5 km, the Z_{DR} peak is only 0.6 dB while the fall speed is about 1.1 m s^{-1} . This suggests that riming may have been occurring throughout the column. Physically, reduction in Z_{DR} by riming makes sense as riming of any oblate crystals like dendrites or plates should trend them to become less anisotropic and riming of aggregates should help trend them to more sphere-like as the thickness of all particles increases (Ono, 1969; Lew et al., 1986a,b).

3.3 Group 2: bimodal spectra

To be classified in this group, the presence of a bimodal velocity spectra must be observed on VertiX. Cases may also have fall speeds greater than 2.0 m s^{-1} ; however, this is not a requirement. Because the main mode of the spectra increases to higher fall speeds during the formation of the secondary mode, the presence of a bimodal spectra is used to indicate riming is occurring. Temporal observations of an example case from 1914-1954 UTC on March 28, 2012 are shown in Figure 6 with the cor-

responding velocity spectra in Figure 7.

The overall vertical profiles of radar observations are generally similar to Group 0 events in regions where riming is not occurring. Near -15°C , the Z gradient increases while a local minima in ρ_{HV} and maxima in Z_{DR} is observed. Below this, dominant growth transitions to aggregation leading to an increase in Z and ρ_{HV} while decreasing Z_{DR} . Figure 7 shows that around 2.5 km a bimodal spectra is observed followed by the growth of these new particles to higher fall speeds while generally staying parallel to the main mode. Corresponding to this bimodal spectra, at the same heights, Figure 6 shows an increase in Z_{DR} and a decrease in ρ_{HV} . Finally, as the crystals melt near 0°C , typical bright band signatures are observed but with a lower and broader Z peak, lower ρ_{HV} values, and a significantly higher Z_{DR} peak.

In all cases within this group, the bimodality generally occurs in the -3 to -8°C temperature range. Crystals formed in this temperature range would likely be either needles or plates (Bailey and Hallett, 2009). The polarimetric signatures observed

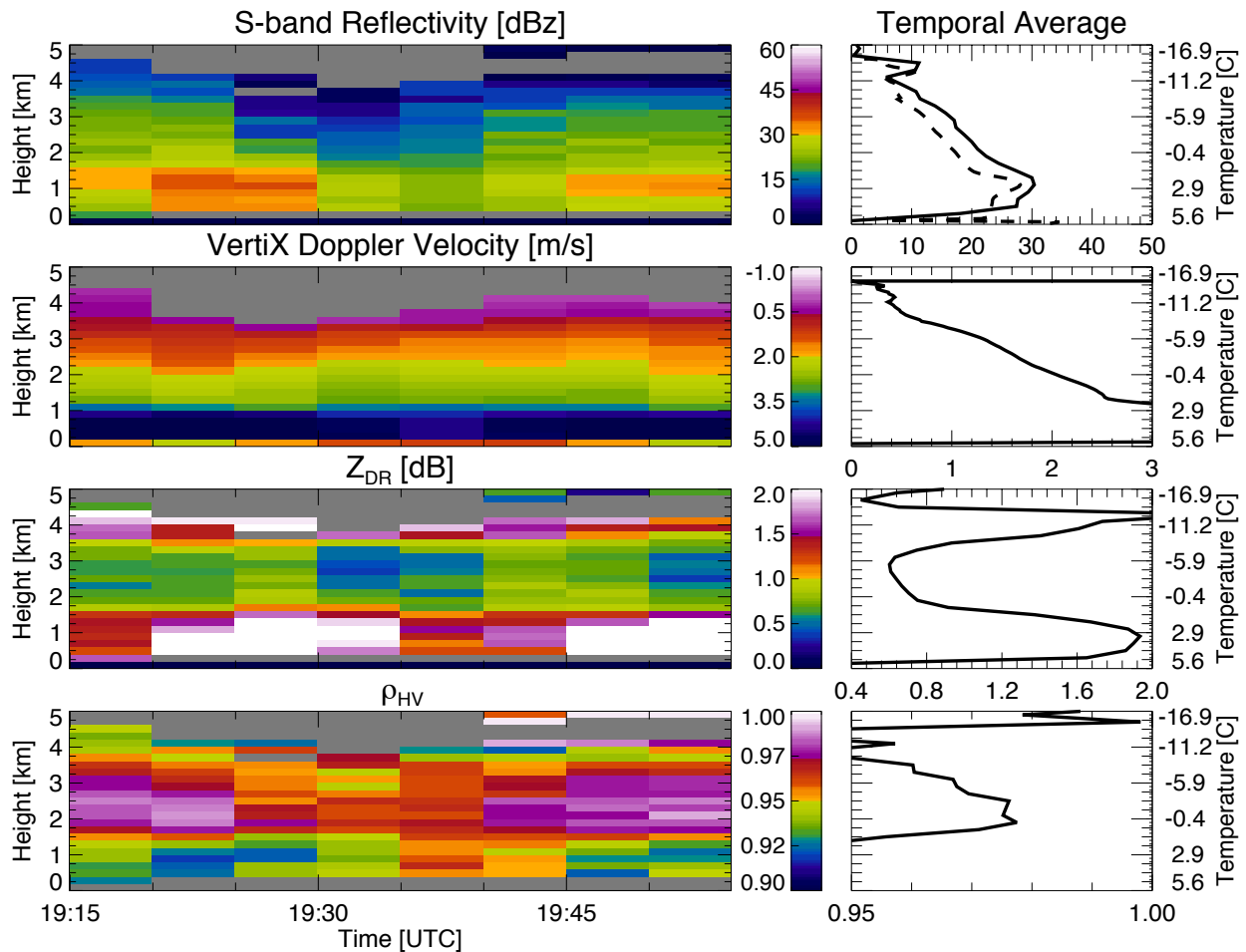


Figure 6: Similar to Figure 2 but for an example of a Group 2 case from 1914-1954 UTC March 28, 2012. The VertiX data has been shifted by 10 minutes to match precipitation timing between the two locations.

make physical sense for the type of crystals formed as small, anisotropic particles would increase Z_{DR} while the variety shapes of crystals present would reduce ρ_{HV} . In other Group 2 cases, the newly formed crystals may grow large and fast enough that their speeds reach the main mode or they are collected by preexisting aggregates. In either of these cases, the local local Z_{DR} maxima and ρ_{HV} minima are observed near where the bimodality appears and disappear near where the bimodality disappears.

3.4 Summary of Radar Observations

Figures 8 & 9 show the averaged vertical profile for all the cases in each of the three groups as well as the standard deviation (Figure 8) and standard error (Figure caseprof). Overall, the vertical profile for the groups generally agrees with previous stud-

ies of polarimetric signatures above the bright band (e.g., Kennedy and Rutledge, 2011; Andrić et al., 2013; Bechini et al., 2013; Schneebeli et al., 2013). In particular, the orange lines in Figure 8 for Group 0 events follow previously documented polarimetric profiles. All three groups show a local maxima in Z_{DR} around the -15°C region corresponding with a local minima in ρ_{HV} . As the dominant growth shifts to aggregation, Z increases, Z_{DR} decreases, and ρ_{HV} increases. The most notable signatures of riming were in Z_{DR} and ρ_{HV} above the bright band. Below about -10°C , bimodal spectra cases (Group 2, red lines) have a higher Z_{DR} and lower ρ_{HV} than non-riming cases (Group 0, orange lines), while riming without bimodal spectra cases (Group 1, blue lines) have lower Z_{DR} and higher ρ_{HV} .

Figure 8 also shows the standard deviation of the mean of the five minute radar scans. Because there is much overlap between each of the three groups

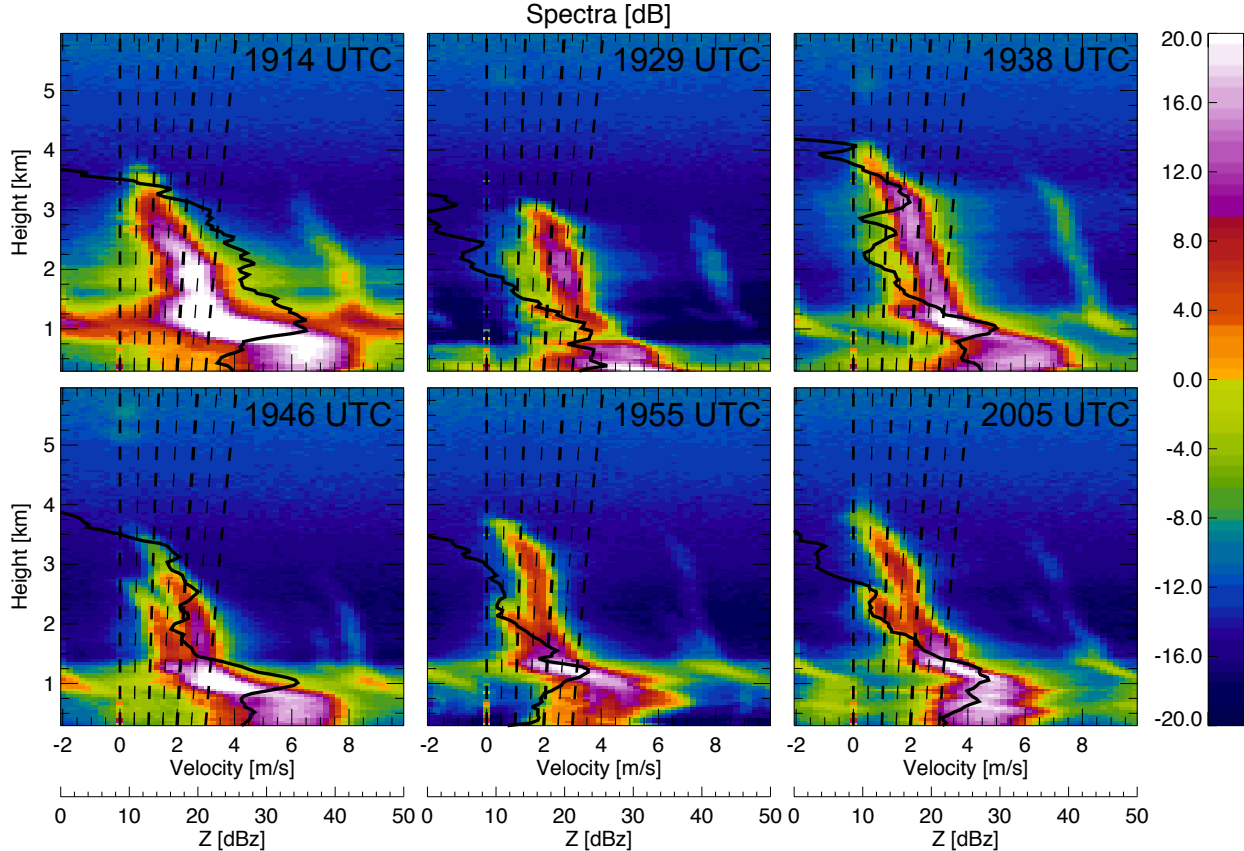


Figure 7: Similar to Figure 3 but for the Group 2 example presented in Figure 6.

(shown in dark green), the signatures are not significant enough to identify riming on a scan by scan basis. However, in Figure 9, at the temperatures typical for riming, there is little to no overlap between groups indicating the signatures, on a case by case basis, are significant enough to identify riming from nonriming events.

Because Z_{DR} above the bright band varied between each of the three groups, Figure 10 shows frequency plots of Z_{DR} versus fall speed between -10°C and the top of the bright band. For comparison purposes, the white line in Figure 10 shows the maximum frequency of Z_{DR} for the Group 0 cases. For Group 1 cases, in regions where riming was occurring, the Z_{DR} was observed to be lower than in Group 0 cases. This is also seen in Figure 10 where the maximum frequency in Z_{DR} is about 0.1 to 0.2 dB lower. For Group 2 cases, in regions where bimodal spectra occur, the Z_{DR} is observed to increase due to the formation of new particles. Figure 10 is in agreement showing the the maximum frequency of Z_{DR} tends to be up to 0.4 dB higher for Group 2 cases.

4 T-MATRIX SCATTERING MODEL

4.1 Model Setup

To help interpret the polarimetric observations, a scattering model by Mishchenko et al. (2000) is used to produce simulated S-band polarimetric values (Lee, 2003). Oblate spheroids are used to represent a variety of ice crystals. For this model, a simplistic approach was chosen where the canting and radar elevation angles were both set to 0° . By this assumption we can obtain the strongest signal one can expect to observe for any of the polarimetric variables. If the signatures are not strong enough under these assumptions, then it can be assumed that the microphysical process will be difficult to observe under real-world conditions with S-band radars.

An exponential size distribution for aggregates and dendrites from Lo and Passarelli (1982) was used as input for the model (Figure 11). Following Kennedy and Rutledge (2011), particles with a diameter of 3 mm or smaller were assumed to be

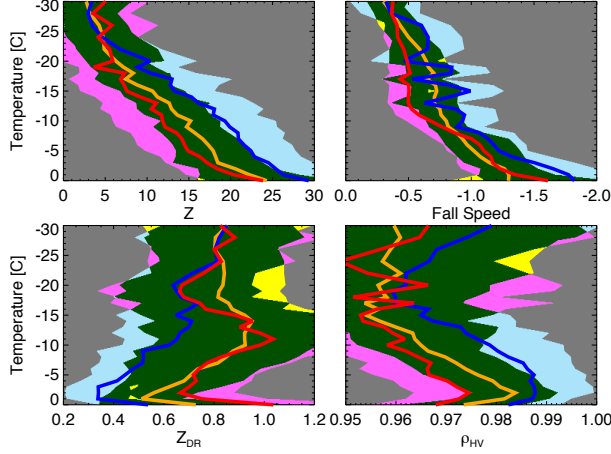


Figure 8: Average vertical profiles of reflectivity, fall speed, Z_{DR} , and ρ_{HV} vs. temperature for all cases: orange for Group 0, blue for Group 1, and red for Group 2. The shading indicates \pm one standard deviation from the mean: yellow for Group 0, light blue for Group 1, magenta for Group 2, and dark green where any of the groups overlap.

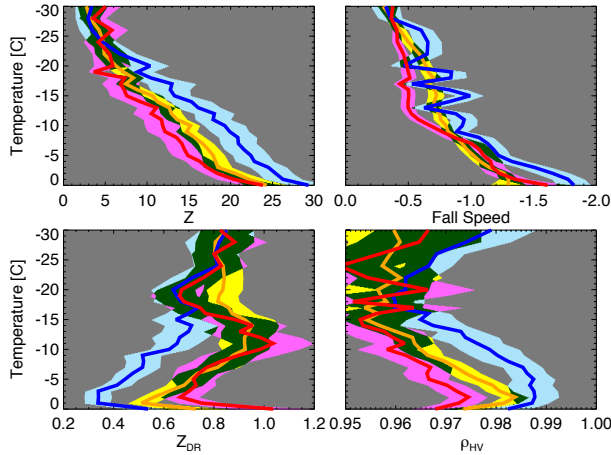


Figure 9: Similar to Figure 8 expect the shading indicates the standard error between cases.

dendrites, while larger particles were assumed to be aggregates. Since our observations of riming generally occur in regions where aggregation is occurring or has taken place, the slope and intercept used were those given in Table 2 of Kennedy and Rutledge (2011).

The mass, terminal velocity, density, and thickness of the particles were calculated using eq. (1) from Andrić et al. (2013). Their values for aggregates, dendrites, and needles were used except for the modifications presented below. The model re-

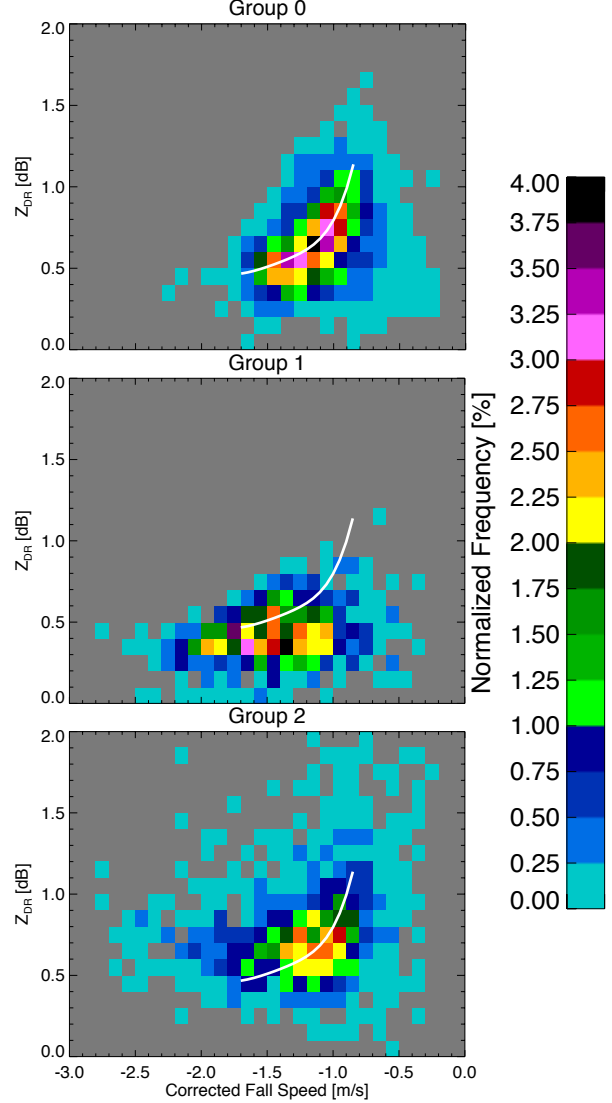


Figure 10: Contours of Z_{DR} vs. fall speed for all cases totalling 63 hours. Data is from above the bright band up to -10°C . The frequency is normalized by the total number of occurrences within each particular group. The white line shows the maximum frequencies for the Group 0 data.

quires the equivalent spherical diameter, axis ratio, and bulk density for each particle. The bulk crystal density is used to calculate the dielectric constant, K^2 , for an air-ice mixture for each size of dendrite or aggregate (Table 3.1 of Fabry, 2015). The axis ratio (AR) is the ratio between the thickness, h in mm, and the longest physical diameter, D in mm, of the crystal, and is calculated by:

$$AR = \frac{h}{D} . \quad (1)$$

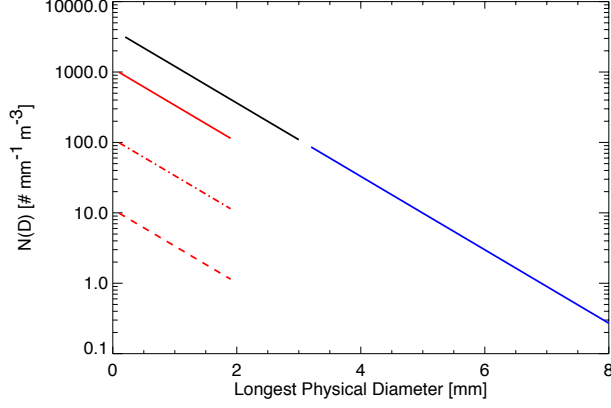


Figure 11: Size distribution from Lo and Passarelli (1982) for the particles used in the T-maxtrix simulation following the methodology of and the slope and intercept from Table 2 of Kennedy and Rutledge (2011). For needles (red lines), three size distributions were tested. For the dashed line, the needle size distribution is assumed to be the same as $N_{aggregate}(D + 5 \text{ mm})$. The dashed-dot and the solid lines represent 10 and 100 times more needles. The black line is for dendrites and blue for aggregates

Because the model will not converge to a solution for very small AR (larger dendrites), the AR was nudged higher for all dendrites by slightly increasing their thickness while preserving the same AR curve shape (Figure 12). The thickness of dendrites is adjusted to:

$$h = 1.835(D/1000)^{0.377} . \quad (2)$$

Since the mass given for dendrites was inconsistent with other observations (Pruppacher and Klett, 1978; Matrosov et al., 1996; Szyrmer and Zawadzki, 2010), the mass, in kg, for dendrites was adjusted to:

$$m = 4.178 \times 10^{-6}(D/10.0)^{2.0} . \quad (3)$$

Additionally, since most aggregates are not perfect spheres, Figure 13 shows the thickness is adjusted so the AR falls between 0.85 and 0.90 (Table 1 of Kennedy and Rutledge, 2011). The resulting thickness is:

$$h = 990(D/1000)^{1.022} . \quad (4)$$

To test more oblate aggregates, the thickness is further reduced so the AR falls between 0.60 and 0.65, for a thickness given by:

$$h = 700(D/1000)^{1.022} . \quad (5)$$

To simulate riming, the thickness and density of the ice crystals are changed. The thickness is increased by an amount ranging from 0.0 to 0.3 mm

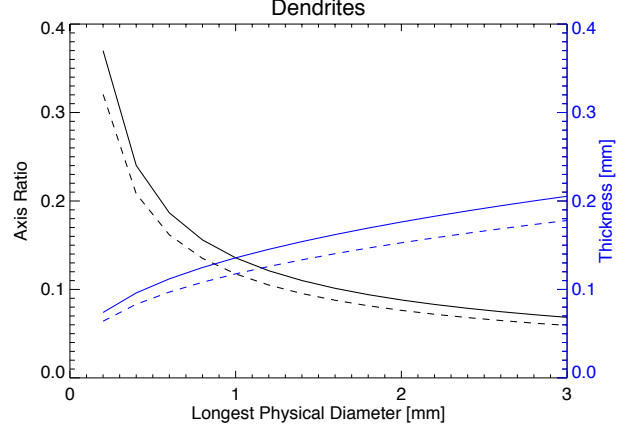


Figure 12: The axis ratio (black lines) and corresponding thickness (blue lines) for dendrites used in the scattering model. Dashed lines represent the values calculated using eq. (1) from Andrić et al. (2013) while solid lines give the adjusted values needed for model convergence.

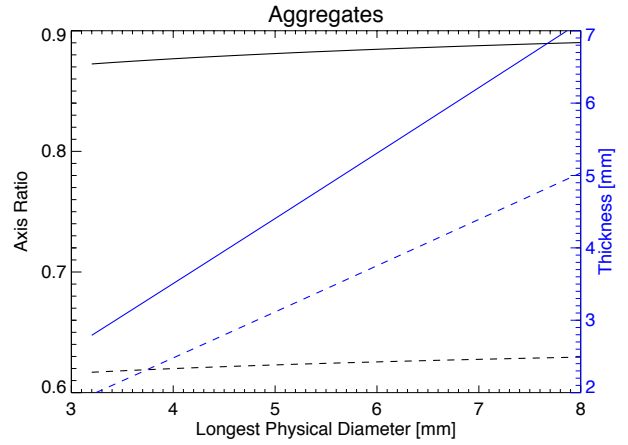


Figure 13: The axis ratio (black lines) and corresponding thickness (blue lines) for aggregates used in the scattering model. Solid lines correspond to aggregates with 0.85 to 0.90 AR, while dashed lines correspond to aggregates with 0.60 to 0.65 AR.

in 0.05 mm increments to simulate the addition of layers of droplets. The 0.05 mm increment is of the order of the diameter of large cloud droplets or collected rime droplets previously observed (Ono, 1969; Wilkins and Auer, 1970; Rogers and Yau, 1989). The volume added due to the thickness increase is then filled with rime droplets varying from 0 to 100% of the added volume in 25% increments while the rest of the added volume is assumed to be air. This is done to simulate the extent of riming from a light coating up to graupel-like. The increase

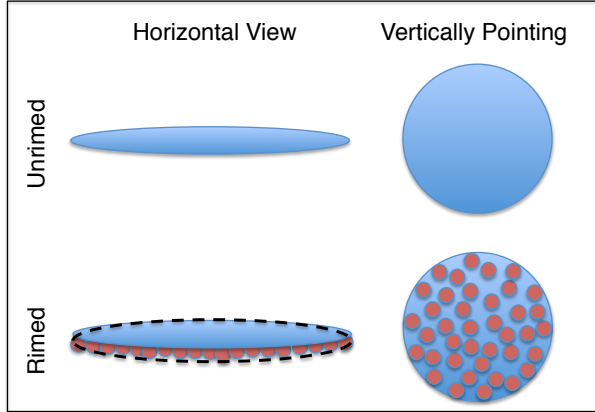


Figure 14: A schematic on how a rimed and unrimed oblate particle may be represented in the T-matrix model. The blue ellipses represent the original ice crystal, the red circles are rime droplets, and the dashed black ellipse represents how the model views a rimed particle.

in volume, V_r , and the increase in mass, M_r , due to riming is added to that of the original ice crystal to get the total mass, M_t , and volume, V_t , which are used to calculate the new density of the ice crystal and its K^2 value. The thickness increase is used to calculate the new AR of the ice crystal. The model is then rerun, assuming all crystals have rimed at the same rate, to calculate the new polarimetric values. Since our cases take place during stratiform precipitation events, rather than during convective events when graupel is likely, it is unlikely for the rimed volume to be completely filled with droplets. Therefore, we have chosen only to show the riming simulations with 50% of the rimed volume filled with droplets. A schematic of this can be seen in Figure 14.

Using equations (1a), (1b), and (23) from Szyrmer and Zawadzki (2010), it was found that tripling the mass of the ice crystal increased the velocity by a factor of about 1.6. Increasing the fall speed of aggregates calculated from eq. (1) in Andrić et al. (2013) by a factor of 1.6 produces velocities similar to the fall speeds observed during riming events. Tripling the mass is roughly equivalent to adding between 0.2 mm and 0.25 mm of rime to the aggregates.

To simulate products formed during periods of bimodal spectra, needle-like oblate spheroids were included. Based on the habit diagram of Bailey and Hallett (2009), needles or plates may be produced in these bimodal regions. For the size ranges given in Table 3 in Andrić et al. (2013) and using their eq. (1) to calculate fall speeds, needles are the most

likely to achieve the fall speeds observed in the secondary spectra. Three different number concentrations of needles were tested (Figure 11).

In an attempt to understand which crystal types produce which signatures when rimed as well as to replicate the observed signatures, several different simulations were run including: only dendrites, only aggregates, aggregates and dendrites, aggregates with needles, and aggregates and dendrites with needles. Simulations of only aggregates or dendrites will allow for an understanding of how each crystal type and size impacts polarimetric signatures. Next, to recreate the observed profiles, different combinations of dendrites, aggregates, and needles were used and then rimed. To replicate the -15°C region, a habit of primarily dendrites with a few aggregates was used. Then, for regions around -5°C , a habit of primarily aggregates with some dendrites was used to recreate Groups 0 and 1 and a habit of aggregates with some dendrites and the addition of needles was used to recreate Group 2. The following section discusses the results of individual crystals as well as collections of a variety of crystals.

4.2 Model Output

4.2.1 Dendrites

To simulate radar signatures from dendrites, the model was run with only a distribution of dendrites: first with only dendrites of an indicated physical diameter (Figure 15a & 15b), then, with a collection of dendrites less than or equal to the indicated physical diameter (Figure 15c & 15d). In the -15°C region, we expect the observations to be dominated by dendritic growth. Figure 8 shows Z in the region ranges between 10-15 dBZ while Z_{DR} ranges from 0.6-1.0 dB. For modelled unrimed dendrites, the black lines in Figures 15c and 15d show Z up to 10 dBZ and Z_{DR} of 4.0 dB. While canting should reduce the Z_{DR} , a simulation canting all dendrites in the habit by the same amount resulted in Z_{DR} values still much higher than observed. However, adding smaller aggregates to the habit (up to a physical diameter of 4.4 mm, not shown) did result in producing similar modelled Z and Z_{DR} values to that around -15°C in Figure 8.

In regions where riming is taking place, it is unlikely that all crystals present are aggregates, so it is useful to simulate the signatures expected from rimed dendrites. The colored lines in Figure 15 show riming in 0.05 mm thickness intervals. While Z increases with riming, the Z_{DR} decreases because the thickness change due to riming domi-

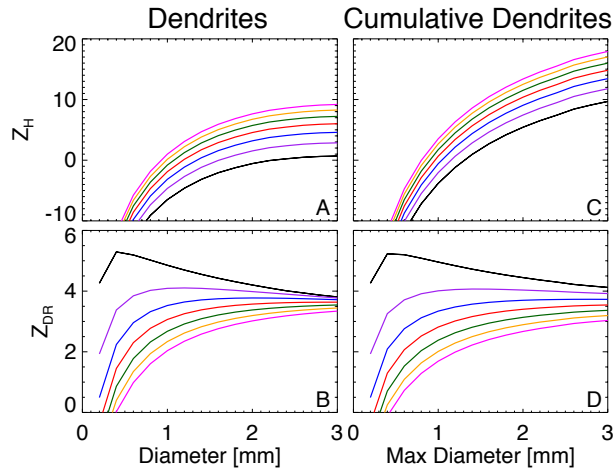


Figure 15: T-matrix simulations for dendrites of the indicated physical diameter (A and B) and for a collection of dendrites up to the physical diameter indicated (C and D). A and C show reflectivity while B and D show Z_{DR} . Colors from black to red to magenta show increasing amounts of riming from 0.0 to 0.15 to 0.30 mm respectively in 0.05 mm increments. Riming simulated in this figure is for 50% of the rimed volume filled with droplets.

nates over the addition of mass.

4.2.2 Aggregates

Next, to simulate radar signatures of aggregates, the model was run with only a distribution of aggregates: first, with only aggregates of the indicated physical diameter (Figure 16ab & 17ab), then, with a collection of aggregates less than or equal to the indicated physical diameter (Figure 16cd & 17cd). This was repeated twice, once for less oblate aggregates with an AR between 0.85 and 0.90 (Figure 16), and once for more oblate aggregates with an AR between 0.60 and 0.65 (Figure 17). For the less oblate aggregates, the model shows that as the extent of riming increases Z_{DR} initially increases but transitions to decreasing as the extent of riming continues to increase. For more oblate aggregates, the model shows that Z_{DR} increases as riming increases. Increases in Z_{DR} are dominated by adding mass by riming while decreases in Z_{DR} are dominated by thickness increases due to riming. For both types of aggregates, however, the changes to Z_{DR} are less than 0.1 dB which are generally too low to be routinely identified with S-band radars.

In the region between -10°C and the bright band, we can expect observations to become increasingly dominated by growth by aggregation. Z values are around 18 dBZ increasing up to 28 dBZ due to rim-

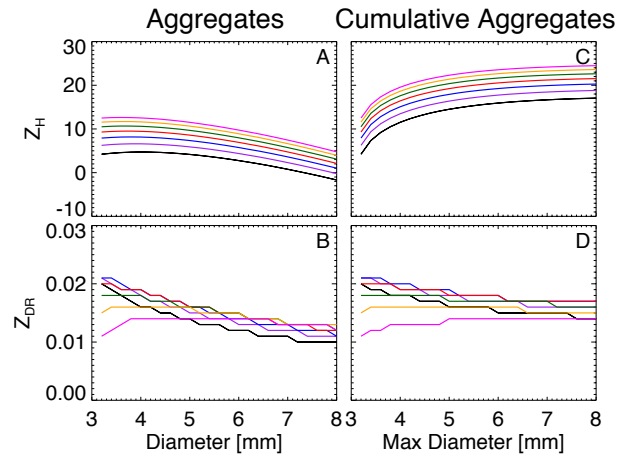


Figure 16: Similar to Figure 15 except for aggregates with an AR between 0.85 to 0.90.

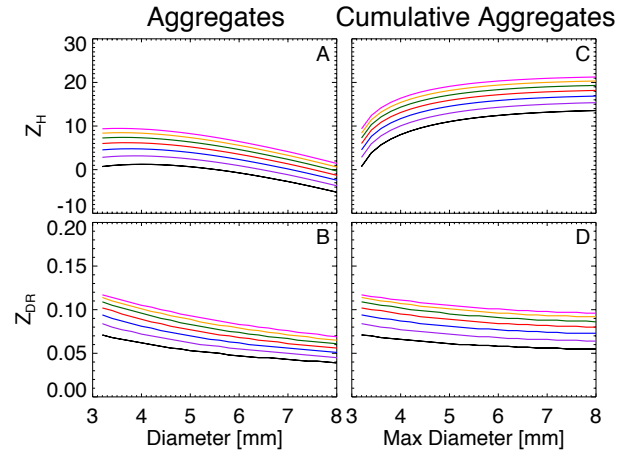


Figure 17: Similar to Figure 15 except for aggregates with an AR between 0.60 to 0.65.

ing while Z_{DR} values are about 0.5 to 0.6 dB decreasing to about 0.3 dB due to riming (orange and blue profiles in Figure 8). Based on modelled results, more spherical aggregates produce a similar Z while both types of aggregates produce a Z_{DR} much lower than observed. Therefore, it is likely that a combination of aggregates and dendrites are present, which will be discussed later.

4.2.3 Needles

Since bimodal spectra are typically observed at temperatures where growth is dominated by aggregates, simulations were conducted with the same habit of aggregates as in the previous section but with the addition of needles. To simulate the ef-

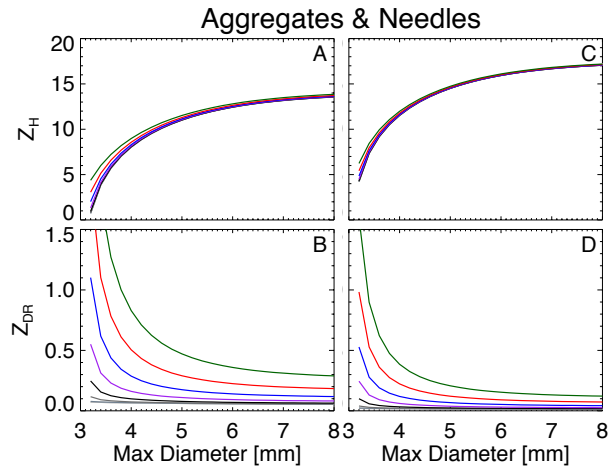


Figure 18: T-matrix simulations for a collection of unrimed aggregates up to the physical diameter indicated. The colored lines indicate a collection of needles with increasing maximum diameter in 0.2 mm increments. The grey lines are for distributions with needles 0.9 mm or less. Colored lines from black to green show distributions with the maximum physical needle length for 1.1 to 1.9 mm, respectively, in 0.2 mm increments. A and C show reflectivity while B and D show Z_{DR} . A and B are for aggregates with AR between 0.60 and 0.65 while C and D are for aggregates with AR between 0.85 and 0.90.

fect needles have on the polarimetric signatures, only unrimed aggregates were used and needles were added in increments of size bins with a longest physical dimension of 0.1 to 1.9 mm in 0.2 mm increments. Each of the needle size distributions (red lines in Figure 11) were tested. From the smallest to largest size distribution of needles, less than a 1 dB increase in Z was seen in the presence of aggregates, while only the highest amount of needles produced a noticeable change in Z_{DR} .

Since the smaller concentrations of needles had a negligible impact on polarimetric variables, only simulations for the largest size distribution of needles are shown. Figure 18 shows that needles have a minimal impact on reflectivity, while, depending on the maximum size of needles, they can increase the Z_{DR} by about 0.1 to 0.3 dB. Needles below 0.9 mm in diameter have a negligible impact on the polarimetric variables; it is not until they grow larger that a signature can be observed. Together, aggregates and needles do not fully reproduce the signature expected for Group 2 (Figure 8); therefore, it is likely that some dendrites may not have aggregated and are still present in the habit, which is discussed in the next section.

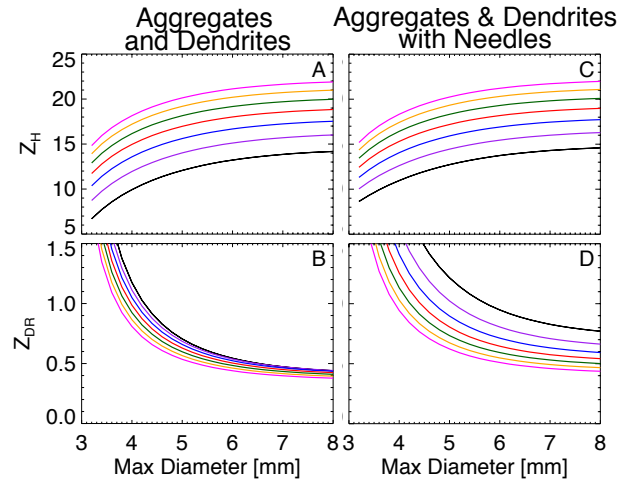


Figure 19: T-matrix simulations for a variety of crystals. A and B are for a combination of aggregates and dendrites; C and D are for a combination of aggregates, dendrites, and needles. A and C show reflectivity while B and D show Z_{DR} . Colors from black to red to magenta show increasing amounts of riming from 0.0 to 0.15 to 0.30 mm respectively in 0.05 mm increments where only the aggregates and dendrites are rimed and 50% of the rimed volume filled with droplets. For A and B (C and D) the amount and physical diameter of dendrites (dendrites and needles) are kept constant at 0 to 2.0 mm; the maximum physical diameter of aggregates varies according to the X-axis.

4.2.4 Combination of Crystals

Based on the individual T-matrix simulations for different types of crystals presented above, we can infer what crystals are the most probable source of the observed signatures in Figure 8. To verify this, additional simulations were run: one with a combination of aggregates and dendrites, another with a combination of aggregates, dendrites, and needles (Figure 19). In these simulations, the aggregates and dendrites were rimed as described above but the needles were not. Since aggregates with an AR between 0.60 and 0.65 produced results more similar to observations, these figures only depict habits with those aggregates.

First, a T-matrix simulation for a habit consisting of a collection of aggregates less than or equal to the indicated physical diameter and a collection of dendrites between 0.2 and 2.0 mm was run. For unrimed conditions (black line in Figure 19A&B), this combination produced results similar to the average Group 0 profile at temperatures warmer than -10°C (orange lines in Figure 8) with Z of about 15 dBZ and Z_{DR} of about 0.4 dB. As this collection of den-

drites and aggregates rime, Z increases to about 22 dBZ and Z_{DR} decreases by about 0.1 dB to 0.3 dB. This is similar to the average Group 1 profile (blue lines in Figure 8).

Next, a T-matrix simulation was conducted for a habit consisting of a collection of aggregates less than or equal to the indicated physical diameter, a collection of dendrites between 0.2 and 2.0 mm, and a collection of needles between 0.1 and 1.9 mm. While the unrimed reflectivity is similar, the Z_{DR} is about 0.3 dB higher (black line in Figure 19C&D) than observations. As the aggregates and dendrites rime, the reflectivity increases up to 22 dBZ while the Z_{DR} decreases to about 0.4 dB. While for this habit, the Z_{DR} decreases with increasing riming due the rimed aggregates and dendrites beginning to dominate, the presence of the needles produces a Z_{DR} signature that is higher than for the habit without needles, as is expected from the average Group 2 profile (red lines in Figure 8).

4.3 Summary of T-matrix Simulations

Simulations of riming of dendrites, riming of aggregates, needles in the presence of aggregates, and combinations of the three were conducted with a T-matrix scattering model. Riming was conducted by increasing the thickness of the crystals in 0.05 mm increments up to 0.30 mm. The volume added due to the thickness increase is then filled with rime droplets varying from 0 to 100% in 25% increments. Because we are not dealing with convective events nor do we expect graupel-like riming, we have only shown the 50% riming cases.

Riming of aggregates was shown to increase Z by less than 10 dB. For rimed aggregates, changes to Z_{DR} depend on the AR of the aggregates. Regardless, riming of aggregates alone produces a change to Z_{DR} less than 0.1 dB, indicating that aggregates alone do not produce the signatures observed by the radar. For dendrites, riming results in an increase in Z and a decrease in Z_{DR} . The simulated values of Z_{DR} for dendrites is much larger than observed indicating a habit entirely of dendrites is unlikely. Adding needles to a habit of aggregates does little to change the Z but does increase the Z_{DR} by a few tenths of a dB. While these tests give indications of what crystals are likely causing the signatures we observe, they do not perfectly replicate those observations. Therefore, a variety of crystal types was used.

Using aggregates and dendrites together replicated the profile seen for Group 0 (orange lines in

Figure 8). When they were rimed, the model produced changes to Z and Z_{DR} similar to that observed for Group 1 (blue lines in Figure 8). Adding needles to the habit of aggregates and dendrites increases the Z_{DR} . While this Z_{DR} decreases due to riming, it is still similar to that observed for Group 2 (red lines in Figure 8). Simulations with higher percentages of riming ($> 50\%$, not shown) lead to dendrites making up a larger portion of the total simulated Z and a faster increase in Z than observed due to the increase in density of the crystals. This also produced a slower decrease in Z_{DR} for dendrites, leading to a simulated Z_{DR} a few tenths of a dB higher for mixed habits.

All these simulations were conducted to show idealistic results for these habits, which are ones without the effects of canting and viewing angles. In a real world case, adding these factors would reduce the simulated signatures. Although these simulations portray highly idealized situations, they do reproduce most of the observations and confirm that the expected signature of riming in widespread rain is at most a few tenths of a dB in Z_{DR} .

5 SUMMARY AND CONCLUSIONS

Using the vertically pointing VertiX and scanning polarimetric S-band radars, three distinct groups have been identified pertaining to riming: no riming, riming without bimodal spectra, and riming with bimodal spectra. Cases were arranged into these three groups based on fall speed and Doppler spectra observations with the VertiX. Then, polarimetric signatures were identified for each group. Finally, the signatures were verified using an idealistic T-matrix model setup. Non-riming cases exhibited profiles of polarimetric variables that have been previously identified in numerous other studies.

Riming without bimodal spectra showed the existence of Z_{DR} signatures lower than that observed in a non-riming event above the bright band. Additionally, the bright band was wider with a weaker Z peak to rain. Based on T-matrix simulations, riming of aggregates would produce signatures too low to be confidently identified by our S-band radar. The simulations suggest that the Z_{DR} signatures observed in this group are most likely due to the riming of smaller dendrites that were not collected by aggregates within the habit.

For cases where a bimodal spectra was present, an increase in Z_{DR} and a decrease in ρ_{HV} was observed at the same altitudes as the beginning of the bimodality. For these cases, the bright band was also wider, with a weaker Z peak to rain, and higher

Z_{DR} . The bimodal spectra indicates the formation of new particles, likely needles or plates at this temperature range. T-matrix simulations of habits that include needles support these observations of increased Z_{DR} .

Z_{DR} values above the bright band in regions where riming is occurring is the main polarimetric variable that varies consistently between all three groups. Cases with a bimodal spectra can have Z_{DR} values of about 0.2 dB up to 0.4 dB higher than non-riming cases while riming cases without a bimodal spectra can have Z_{DR} values up to 0.2 dB lower than non-riming events. However, Table 6.5 in Lee (2003) has shown the measurement noise for Z_{DR} is around 0.33 dB and the total standard deviation is around 0.35 dB (Lee, 2006). The observations given here were averaged over the region in Figure 1 with the hope to reduce error. But, Cunningham et al. (2013) and Ice et al. (2014) have shown a systematic Z_{DR} bias for the NEXRAD network of several tenths of a dB. While we can infer riming with the VertiX, it appears that for our S-band radar these signatures are not significant enough to detect riming without the presence of another aid, such as a vertically pointing radar.

ACKNOWLEDGEMENTS

This project was undertaken with the financial support of the Government of Canada provided through the Department of the Environment and the Natural Sciences and Engineering Research Council of Canada. The first author thanks Alamelu Kilambi for help accessing the McGill radar data and Bernat Puigdomènech Treserras for help processing the radar data.

REFERENCES

- Andrić, J., M. R. Kumjian, D. S. Zrnić, J. M. Straka, and V. M. Melnikov, 2013: Polarimetric signatures above the melting layer in winter storms: An observational and modeling study. *J. Appl. Meteor. Climatol.*, **52**, 682–700.
- Bailey, M. P., and J. Hallett, 2009: A comprehensive habit diagram for atmospheric ice crystals: Confirmation from the laboratory, air, and other field studies. *J. Atmos. Sci.*, **66**, 2888–2899.
- Barthazy, E., and R. Schefold, 2006: Fall velocity of snowflakes of different riming degree and crystal types. *Atmos. Res.*, **82**, 391–398.
- Bechini, R., L. Baldini, and V. Chandrasekar, 2013: Polarimetric radar observations in the ice region of precipitating clouds at c-band and x-band radar frequencies. *J. Appl. Meteor. Climatol.*, **52**, 1147–1169.
- Brandes, E. A., K. Ikeda, G. Thompson, and M. Schönhuber, 2008: Aggregate terminal velocity/temperature relations. *J. Appl. Meteor. Climatol.*, **47**, 2729–2736.
- Byers, H. R., 1965: *Elements of Cloud Physics*. University of Chicago Press, 191 pp.
- Cunningham, J. G., W. D. Zittle, R. R. Lee, and R. L. Ice, 2013: Methods for identifying systematic differential reflectivity (zdr) biases on the operational wsr-88d network. *36th Conference on Radar Meteorology*, Breckenridge, CO, USA.
- Fabry, F., 2015: *Radar Meteorology: Principles and Practice*. Cambridge University Press, 253 pp.
- Fabry, F., and I. Zawadzki, 1995: Long-term radar observations of the melting layer of precipitation and their interpretation. *J. Atmos. Sci.*, **52**, 838–851.
- Fabry, F., and I. Zawadzki, 2000: Atmospheric physics as observed by a vertically pointing doppler radar. *13th International Conference on Clouds and Precipitation*, Reno, NV, USA.
- Hallett, J., and S. C. Mossop, 1974: Production of secondary ice particles during the riming process. *Nature*, **249**, 26–28.
- Holleman, I., A. Huuskonen, R. Gill, and P. Tabary, 2010: Operational monitoring of radar differential reflectivity using the sun. *J. Atmos. Oceanic Technol.*, **27**, 881–887.
- Ice, R. L., J. G. Cunningham, and J. N. Christman, 2014: Improving and exploiting polarimetric weather radar data – plans and status. *30th Conference on Environmental Information Processing Technologies*, Atlanta, GA, USA.
- Illingworth, A. J., J. W. F. Goddard, and S. M. Cherry, 1987: Polarization radar studies of precipitation development in convective storms. *Quart. J. Roy. Meteor. Soc.*, **113**, 469–489.
- Kennedy, P. C., and S. A. Rutledge, 2011: S-band dual-polarization radar observations of winter storms. *J. Appl. Meteor. Climatol.*, **50**, 844–858.

- Kumjian, M. R., A. P. Khain, N. Benmoshe, E. Iloviz, A. V. Ryzhkov, and V. T. J. Phillips, 2014: The anatomy and physics of zdr columns: Investigating a polarimetric radar signature with a spectral bin microphysical model. *J. Appl. Meteor. Climatol.*, **53**, 1820–1843.
- Kumjian, M. R., A. V. Ryzhkov, H. D. Reeves, and T. J. Schuur, 2013: A dual-polarization radar signature of hydrometeor refreezing in winter storms. *J. Appl. Meteor. Climatol.*, **52**, 2549–2566.
- Lee, G. W., 2003: Errors in rain measurement by radar: effect of variability of drop size distributions. Ph.D. thesis, McGill University, Montreal, Quebec, Canada.
- Lee, G. W., 2006: Sources of errors in rainfall measurements by polarimetric radar: Variability of drop size distributions, observational noise, and variation of relationships between r and polarimetric parameters. *J. Atmos. Oceanic Technol.*, **23**, 1005–1028.
- Lew, J. K., D. C. Montague, H. R. Pruppacher, and R. M. Rasmussen, 1986a: A wind tunnel investigation on the riming of snowflakes. part i: Porous disks and large stellars. *J. Atmos. Sci.*, **43**, 2392–2409.
- Lew, J. K., D. C. Montague, H. R. Pruppacher, and R. M. Rasmussen, 1986b: A wind tunnel investigation on the riming of snowflakes. part ii: Natural and synthetic aggregates. *J. Atmos. Sci.*, **43**, 2410–2417.
- Lo, K. K., and R. E. Passarelli, 1982: The growth of snow in winter storms: an airborne observational study. *J. Atmos. Sci.*, **39**, 697–706.
- Matrosov, S. Y., R. F. Reinking, R. A. Kropfli, and B. W. Bartram, 1996: Estimation of ice hydrometeor types and shapes from radar polarization measurements. *J. Atmos. Oceanic Technol.*, **13**, 85–96.
- Mishchenko, M. I., J. W. Hovenier, and L. D. Travis, 2000: *Light Scattering by Nonspherical Particles: Theory, Measurements, and Applications*. Academic Press, 690 pp.
- Mosimann, L., 1995: An improved method for determining the degree of snow crystal riming by vertical doppler radar. *Atmos. Res.*, **37**, 305–323.
- Mosimann, L., M. Steiner, and W. Henrich, 1993: Prediction of snow crystal shape and riming by vertical doppler radar. *Atmos. Res.*, **29**, 85–98.
- Ono, A., 1969: The shape and riming properties of ice crystals in natural clouds. *J. Atmos. Sci.*, **26**, 138–147.
- Pruppacher, H. R., and J. D. Klett, 1978: *Microphysics of Clouds and Precipitation*. D. Reidel, 714 pp.
- Rogers, R. R., and M. K. Yau, 1989: *A Short Course in Cloud Physics*. 3rd ed., Pergamon Press, 304 pp.
- Ryzhkov, A. V., and D. S. Zrnic, 1998: Discrimination between rain and snow with a polarimetric radar. *J. Appl. Meteor.*, **37**, 1228–1240.
- Schneebeli, M., N. Dawes, M. Lehning, and A. Berne, 2013: High-resolution vertical profiles of x-band polarimetric radar observables during snowfall in the swiss alps. *J. Appl. Meteor. Climatol.*, **52**, 378–394.
- Szyrmer, W., and I. Zawadzki, 2010: Snow studies. part ii: Average relationship between mass of snowflakes and their terminal fall velocity. *J. Atmos. Sci.*, **67**, 3319–3335.
- Wilkins, R. D., and A. H. Auer, 1970: Riming properties of hexagonal ice crystals. *Conference on Cloud Physics*, Ft. Collins, CO, USA, American Meteorological Society.
- Zawadzki, I., 2013: Observations of snow growth by a vertically pointing radar. *36th Conference on Radar Meteorology*, Breckenridge, CO, USA.
- Zawadzki, I., F. Fabry, and W. Szyrmer, 2001: Observations of supercooled water and secondary ice generation by a vertically pointing x-band doppler radar. *Atmos. Res.*, **59–60**, 343–359.
- Zawadzki, I., W. Szyrmer, C. Bell, and F. Fabry, 2005: Modeling of the melting layer. part iii: The density effect. *J. Atmos. Sci.*, **62**, 3705–3723.
- Zawadzki, I., W. Szyrmer, and S. Laroche, 2000: Diagnostic of supercooled clouds from single-doppler observations in regions of radar-detectable snow. *J. Appl. Meteor.*, **39**, 1041–1058.